Monthly Notices
of the
ROYAL ASTRONOMICAL SOCIETY

MNRAS **439,** 3439–3452 (2014)
Advance Access publication 2014 February 25

doi:10.1093/mnras/stu191

Cumulative luminosity distributions of supergiant fast X-ray transients in hard X-rays

A. Paizis★ and L. Sidoli

INAF, Istituto di Astrofisica Spaziale e Fisica Cosmica, Via E. Bassini 15, I-20133 Milano, Italy

Accepted 2014 January 24. Received 2014 January 24; in original form 2013 November 15

ABSTRACT

We have analysed in a systematic way about nine years of *INTEGRAL* data (17–100 keV) focusing on supergiant fast X-ray transients (SFXTs) and three classical high-mass X-ray binaries (HMXBs). Our approach has been twofold: image-based analysis, sampled over a ∼ks time frame to investigate the long-term properties of the sources and light-curve-based analysis, sampled over a 100 s time frame to seize the fast variability of each source during its ∼ ks activity. We find that while the prototypical SFXTs (IGR J17544−2619, XTE J1739−302 and SAX J1818.6−1703) are among the sources with the lowest ∼ ks-based duty cycle (<1 per cent activity over nine years of data), when studied at the 100 s level, they are the ones with the highest detection percentage, meaning that, when active, they tend to have many bright short-term flares with respect to the other SFXTs. To investigate in a coherent and self-consistent way all the available results within a physical scenario, we have extracted cumulative luminosity distributions for all the sources of the sample. The characterization of such distributions in hard X-rays, presented for the first time in this work for the SFXTs, shows that a power-law model is a plausible representation for SFXTs, while it can only reproduce the very high luminosity tail of the classical HMXBs, and even then, with a significantly steeper power-law slope with respect to SFXTs. The physical implications of these results within the frame of accretion in wind-fed systems are discussed.

Key words: accretion, accretion discs – stars: neutron – X-rays: binaries – X-rays: individual: IGR J17544−2619 – X-rays: individual: SAX J1818.6−1703 – X-rays: individual: XTE J1739−302.

1 INTRODUCTION

The *INTErnational Gamma-Ray Astrophysics Laboratory* (*INTEGRAL*; Winkler et al. 2003, 2011) is a medium-sized ESA mission successfully launched in 2002. Thanks to its large field of view, sensitivity at hard X-rays and observing strategy, it is optimized to surveying the hard X-ray sky. It has currently discovered about six hundred new sources.[1] Among these, several display extreme transient behaviour, with recurrent bright X-ray flares (reaching peak luminosities around 10^{36}–10^{37} erg s^{-1}) of short duration (from a few minutes to a few hours; Sguera et al. 2005; Negueruela et al. 2006a). These luminous and brief X-ray flares compose major outbursts lasting a few days (with the brightest accretion phase typically lasting ∼ one day or less; Romano et al. 2007), spaced by a very variable time interval, ranging from a few weeks to several months (e.g. Blay et al. 2008).

These hard transients, optically associated with early-type supergiant companions, were called supergiant fast X-ray transients (SFXTs). SFXTs are high-mass X-ray binaries (HMXBs) hosting a compact object, normally a neutron star (NS), accreting mass from the wind of the supergiant donor which underfills its Roche lobe (see Sidoli 2013 for a recent review). The most controversial issues related to SFXTs deal with two aspects: the physical mechanism producing their sporadic transient X-ray emission during outbursts (which remain unpredictable, except for the periodic SFXT IGR J11215−5952, Sidoli et al. 2006) and the link with more classical HMXBs, discovered in the early days of X-ray astronomy, where the X-ray emission is persistent (e.g. Vela X-1, 4U 1700−377).

In orbit since 2002, *INTEGRAL* allowed us to build a large data base (Paizis et al. 2013) which enables a statistical approach to explore the SFXT extreme phenomena and their link to the more classical HMXBs.

In this paper, we used the long-based *INTEGRAL* archival data of all known SFXTs to fully characterize for the first time their hard X-ray (17–100 keV) transient emission, by means of the cumulative luminosity distribution of their SFXT flares. We compared their

★ E-mail: ada@iasf-milano.inaf.it

[1] See e.g. http://irfu.cea.fr/Sap/IGR-Sources/

Table 1. The sources studied in this work, together with their main characteristics.

Name	Companion	Distance (kpc)	Orbital period (d)	Spin period (s)	Superorbital period (d)
Prototypical SFXTs					
XTE J1739−302	O8Iab(f) (1, 2)	2.7 (2)	51.47 ± 0.02 (3)		
IGR J17544−2619	O9Ib (4)	3.6 (2, 4)	4.926 ± 0.001 (5)	71.49 ±0.02 (6)	
SAX J1818.6−1703	∼B0I (7, 8)	2, 2.1 (8, 9)	30.0 ± 0.2 (10, 11)		
Intermediate SFXTs					
IGR J16418−4532	OB Sg	13 (12)	3.753 ± 0.004 (13)	1212 ± 6 (14)	14.6842 ± 0.0008 (15, 16)
IGR J16479−4514	O8.5I, O9.5Iab (2, 17)	4.9, 2.8 (2, 17)	3.3194 ± 0.001 (18, 19)		11.880 ± 0.002 (15, 16)
IGR J18483−0311	B0.5Ia (20)	3 (20)	18.55 ± 0.03 (21)	21.0526 ± 0.0005 (22)	
IGR J18450−0435	O9.5I (23)	3.6 (23)	5.7195 ± 0.0007 (24)		
Less explored SFXTs					
IGR J16465−4507	O9.5Ia (23)	$9.5\ ^{+14.1}_{-5.7}$ (23)	30.243 ± 0.035 (25, 26)	228 ± 6 (27)	
IGR J08408−4503	O8.5Ib (28)	2.7 (29)			
IGR J18410−0535	B1Ib (17)	$3.2\ ^{+2.0}_{-1.5}$ (23)			
The periodic SFXT					
IGR J11215−5952	B0.5Ia (30, 31)	6.2, 8 (32, 30)	164.6 (34, 35)	186.78 ± 0.3 (36)	
HMXBs					
4U 1700−377	O6.5Iaf+ (37)	1.9, 2.1 (37, 38)	3.41161 ± 0.000 05 (39)		13.8 (39)
Vela X-1	B0.5Ib	1.8	8.9 (40)	283 (40)	
4U 1907+09	O8-O9 Ia (41)	2–6	8.38 (42)	437.5 (43)	

(1) Negueruela et al. (2006b), (2) Rahoui et al. (2008), (3) Drave et al. (2010), (4) Pellizza, Chaty & Negueruela (2006), (5) Clark et al. (2009), (6) Drave et al. (2012), (7) Negueruela & Smith (2006) (8) Torrejón et al. (2010), (9) Negueruela, Torrejón & Reig (2008), (10) Zurita Heras & Chaty (2009), (11) Bird et al. (2009), (12) Chaty et al. (2008), (13) Corbet et al. (2006), (14) Sidoli et al. (2012), (15) Corbet & Krimm (2013), (16) Drave et al. (2013), (17) Nespoli, Fabregat & Mennickent (2008), (18) Jain, Paul & Dutta (2009), (19) Romano et al. (2009), (20) Rahoui & Chaty (2008), (21) Levine & Corbet (2006), (22) Sguera et al. (2007), (23) Coe et al. (1996), (24) Goossens et al. (2013), (25) Clark et al. (2010), (26) La Parola et al. (2010), (29) Leyder et al. (2007), (30) Negueruela, Smith & Chaty (2005), (31) Lorenzo, Negueruela & Norton (2010), (32) Masetti et al. (2006), (34) Sidoli, Paizis & Mereghetti (2006), (35) Sidoli et al. (2007), (36) Swank, Smith & Markwardt (2007), (37) Ankay et al. (2001), (38) Megier et al. (2009), (39) Hong & Hailey (2004), (40) McClintock et al. (1976), (41) Cox, Kaper & Mokiem (2005), (42) Marshall & Ricketts (1980) and (43) Makishima et al. (1984).

luminosity distribution with those of three classical HMXB systems, two persistent and one transient. The sources studied in this work and their main properties can be seen in Table 1.

For clarity, we classified the sources considered in the present study into various subtypes ('prototypical', 'intermediate', 'less explored' and 'periodic'), depending on the source properties found in the literature. With 'prototypical SFXTs' we mean the SFXTs which have displayed in the past a very high dynamic range (ratio between the flares luminosity at their peak and the quiescent luminosity), exceeding 10^3; with 'intermediate SFXTs' we mean the SFXTs with a much lower dynamic range of about two orders of magnitude (e.g. Sguera et al. 2008). We designate 'less explored SFXTs' the sources poorly studied in the previous literature, while with 'periodic' we mean the only SFXT with a strictly periodic flaring behaviour, IGR J11215−5952 (Sidoli et al. 2006).

2 DATA ANALYSIS: AN *INTEGRAL* ARCHIVE

The *INTEGRAL* payload consists of two main gamma-ray instruments, the spectrometer SPI (Vedrenne et al. 2003) and the imager IBIS (Ubertini et al. 2003), covering the 15 keV–10 MeV band. IBIS is a high angular resolution gamma-ray imager optimized for accurate point source imaging and for the continuum and broad line spectroscopy. It consists of two layers, the lower energy one (IBIS/ISGRI, 15 keV–1 MeV; Lebrun et al. 2003) and the higher energy one (IBIS/PICsIT, 0.175–10 MeV; Labanti et al. 2003). Co-aligned with SPI and IBIS are two X-ray monitors JEM–X (4–35 keV; Lund et al. 2003) and an optical monitor OMC (500–600 nm; Mas-Hesse et al. 2003). At the time of writing, a total of about 10 years of data have become public and are available to the scientific community. In order to increment and ease our exploitation of *INTEGRAL* data, we undertook the task of preparing and maintaining an *INTEGRAL* archive (Paizis et al. 2013). The scripts we have used to build it are publicly available.[2]

The data used in this study span from revolution 0026 to 1159, i.e. 2002 December–2012 April (90491 pointings). A detailed description of the data analysis and products is given in Paizis et al. (2013). Here only the main information is given, for completeness.

INTEGRAL data are downloaded from the ISDC Data Centre for Astrophysics (former INTEGRAL Science Data Centre) and a customized analysis using the OSA 9.0 software package[3] is routinely performed on the IBIS/ISGRI data.

IBIS is a coded aperture imaging system. In such systems, the source radiation is spatially modulated by a mask of opaque and transparent elements before being recorded by a position sensitive detector. This enables simultaneous measurement of source plus background (through the mask holes) and background fluxes (through the opaque elements). To optimize sky image

[2] http://www.iasf-milano.inaf.it/~ada/GOLIA.html
[3] http://www.isdc.unige.ch/integral/analysis

Table 2. Global view of our IMA analysis results (exposure times are rounded for clarity). No value ('–') means that the source was never detected in the given energy band.

Name	Source $\leq 12^\circ$	Average rate[a] (17–30 keV)	Detections[a] (17–30 keV)	Detections[a] (30–50 keV)	Detections[a] (17–50 keV)	Detections[a] (50–100 keV)
	Ms (#ScWs)	counts s^{-1}	ks (#ScWs)	ks (#ScWs)	ks (#ScWs)	ks (#ScWs)
Prototypical SFXTs						
XTE J1739−302	14.6 (9215)	11.7 ± 0.1	130.7 (70)	95.8 (52)	157.1 (87)	2.5 (1)
IGR J17544−2619	14.3 (9042)	11.2 ± 0.2	103.8 (62)	16.1 (9)	102.6 (64)	1.1 (1)
SAX J1818.6−1703	7.3 (4991)	12.4 ± 0.2	52.1 (34)	24.7 (15)	73.5 (46)	5.0 (2)
Intermediate SFXTs						
IGR J16418−4532	8.0 (5337)	9.0 ± 0.2	71.9 (40)	10.5 (9)	98.0 (57)	–
IGR J16479−4514	7.9 (5255)	8.9 ± 0.1	188.5 (111)	121.0 (75)	291.2 (172)	7.2 (4)
IGR J18483−0311	6.0 (4281)	8.4 ± 0.1	199.5 (126)	110.8 (70)	313.5 (200)	1.1 (1)
IGR J18450−0435	5.7 (3887)	5.7 ± 0.3	13.1 (8)	5.2 (4)	24.0 (16)	–
Less explored SFXTs						
IGR J16465−4507	7.8 (5185)	5.9 ± 0.4	9.8 (6)	3.7 (2)	19.8 (11)	–
IGR J08408−4503	4.5 (2343)	4.7 ± 0.3	7.3 (3)	4.9 (2)	4.9 (2)	–
IGR J18410−0535	5.3 (3887)	8.0 ± 0.3	23.2 (16)	14.6 (12)	38.4 (29)	–
The periodic SFXT						
IGR J11215−5952	4.1 (2052)	6.9 ± 0.3	17.8 (11)	15.0 (9)	35.7 (19)	–
HMXBs						
4U 1700−377	11.0 (7048)	50.91 ± 0.03	8109.96 (5105)	7837.87 (4922)	8348.69 (5285)	5565.39 (3373)
Vela X-1	4.9 (2488)	58.97 ± 0.03	3872.72 (1961)	3819.02 (1927)	3886.44 (1970)	832.3 (363)
4U 1907+09	6.9 (4147)	6.19 ± 0.03	1795.38 (917)	80.2 (35)	1600.32 (815)	–
Crab	4.415 (2897)	172.70 ± 0.03	4415 (2897)	4415 (2897)	4415 (2897)	4415 (2897)

[a]We provide the exposure time, as well as the number of ScWs (#ScWs), in which an IMA significance >5 is obtained.

reconstruction, mask patterns are designed so that each source in the field of view results in a unique shadowgram on the detector. The image reconstruction (deconvolution) is based on a correlation procedure between the recorded image and a decoding array derived from the mask pattern (Goldwurm et al. 2001, 2003). The scientific products include individual pointing images (pointing duration $\sim$ ks) and the associated detected source lists in the selected energy bands. Hereafter we refer to the image deconvolution results as IMA results.

Once the positions of the active sources of the field are known from the IMA step, their fluxes are extracted for each pointing in predefined energy and time bins. This extraction is based on simultaneous fitting of source and background shadowgram models to detector images. Hereafter we refer to the light-curve extraction results as LCR results.

The scientific products obtained in our analysis include individual pointing images and the associated detected source lists in the 17–30, 30–50, 17–50 and 50–100 keV energy bands (IMA results), as well as light curves binned over 100 s in the 17–30 keV band for sources detected in the images (LCR results).

We consider a 5σ detection threshold in the IMA step (in each band) and a 3σ detection threshold in the LCR one (where we know the source to be active from IMA). For SFXTs alone, as a cross-check, we have extracted IMA results in the 22–50 keV band as well, to make sure that the instrumental low threshold fluctuations do not introduce any kind of bias in our results.

In this work we show the overall behaviour of the selected sources in the hard X-ray domain spanning over about nine years, mapping the behaviour of the sources in two time frames: pointing basis ($\sim$ ks, IMA results) and light-curve basis (100 s, LCR results). We have considered only the pointings (or Science Windows, hereafter ScW) in which the sources were within 12° from the centre. Indeed, at larger off-axis angles the IBIS response is not well known and strongly energy dependent, hence systematic flux variations may be introduced.[4] A quick glance at the data between 12° and 20° is however included in Section 3, for completeness.

Besides the sources shown in Table 1, we include the results from the Crab source, that we consider like the 'point spread function' of our archive, to check for the consistency of our analysis.

3 DETECTIONS AND DUTY CYCLES

3.1 IMA results ($\sim$ks sampling)

In Table 2 we present our results from the IMA step. The total exposure time for which each source was within 12° is given, together with the exposure time (and number of ScWs) in which the source was found to be active in each band (IMA significance >5). Most sources have the highest detection rate in the 17–50 keV band, hence this band is the best one to investigate the duty cycles of SFXTs in hard X-rays. Table 3 shows the computed duty cycles for the sources in our sample. We have included the 17–30 keV band as well, for comparison.

[4] http://www.isdc.unige.ch/integral/osa/9.0/issues_osa

Table 3. Obtained IMA duty cycles in the 17–50 and 17–30 keV band.

Name	Duty cycle (per cent)[a] (17–50 keV)	Duty cycle (per cent)[a] (17–30 keV)
Prototypical SFXTs		
XTE J1739−302	1.07	0.89
IGR J17544−2619	0.72	0.72
SAX J1818.6−1703	1.00	0.71
Intermediate SFXTs		
IGR J16418−4532	1.23	0.90
IGR J16479−4514	3.68	2.39
IGR J18483−0311	5.22	3.31
IGR J18450−0435	0.42	0.23
Less explored SFXTs		
IGR J16465−4507	0.25	0.13
IGR J08408−4503	0.11	0.16
IGR J18410−0535	0.72	0.44
The periodic SFXT		
IGR J11215−5952	0.87	0.44
HMXBs		
4U 1700−377	76.0	73.8
Vela X-1	79.4	79.1
4U 1907+09	23.1	26.0
Crab	100	100

[a]Duty cycle (i.e. percentage of source activity computed using the exposure times of Table 2).

3.2 LCR results (100 s sampling)

Once a source is detected in the imaging part, i.e. active in a ScW, a light curve with a 100 s binning is also extracted in the 17–30 keV band. In Table 4 we present our results from the light-curve step. The number of 100 s bins in which the source was within 12° (and active in IMA) is given, together with the number of bins in which there is at least a 3σ detection in a single 100 s bin. The duty cycles (i.e. percentage of source activity at the 100 s level) are also shown. We note here that the results from the light-curve step show the short-term variability *when the source is active at the ScW level*, hence the duty cycles given are not with respect to the whole nine year archive, but with respect to when the source was active in the IMA step (e.g. XTE J1739−302 is detected 27.3 per cent of the times in 100 s bins during its IMA activity).

3.3 The outer part of the field of view

Since spectral analysis and conversion to luminosities are involved in our work, we decided to present our results only within 12°, where the IBIS/ISGRI response is better known and where the signal-to-noise ratio reconstruction is cleaner. A detection of a source beyond 12°, i.e. in the most extreme part of the detector, could be fake and in an archival approach such as ours, it could be misleading. Nevertheless, for completeness, we briefly report here the detections in the outer part of the field of view, namely between 12° and 20°.

The number of ScWs in which the sources are detected at least at 5σ in the 17–50 keV band between 12° and 20° in the images are as follows: 14 for IGR J18483−0311, 12 for SAX J1818.6−1703, 5 for IGR J16479−4514, 2 for XTE J1739−302, 2 for IGR J17544−2619, 1 for IGR J16418−4532, 1 for IGR J11215−5952, 1 for IGR J18450−0435, and 0 for IGR J16465−4507, IGR J08408−4503 and IGR J18410−0535. A detailed analysis of these pointings to assess their true nature is beyond the scope of this paper.

The same 12° radius choice is applicable to the LCR part. Indeed, once we consider a 20° radius, we obtain luminosity distributions unrealistically stretched towards very high luminosities: the Crab distribution is detected at more than 3σ up to 1×10^{37} erg s^{-1}.

Table 4. Global view of our LCR analysis results.

Name	Source ≤12° [a]	Detections[b] (17–30 keV)	Duty cycle[c] (17–30 keV)
	#bins	#bins	per cent
Prototypical SFXTs			
XTE J1739−302	1938	530	27.3
IGR J17544−2619	1589	334	21.0
SAX J1818.6−1703	769	207	26.9
Intermediate SFXTs			
IGR J16418−4532	1097	77	7.0
IGR J16479−4514	2856	319	11.2
IGR J18483−0311	3034	397	13.1
IGR J18450−0435	200	8	4.0
Less explored SFXTs			
IGR J16465−4507	142	7	4.9
IGR J08408−4503	103	17	16.5
IGR J18410−0535	348	60	17.2
The periodic SFXT			
IGR J11215−5952	254	40	15.7
HMXBs			
4U 1700−377	123337	84693	68.7
Vela X-1	57543	52679	91.5
4U 1907+09	26154	3508	13.4
Crab	68543	68246	99.6

[a]Not all bins have exactly 100 s (the last bin of each ScW will be less), hence the correct exposure times of the source within 12° are to be taken from Table 2.
[b]Bin with $\sigma > 3$.
[c]Duty cycle computed using the number of bins.

4 FROM COUNT RATES TO LUMINOSITY

Conversion factors from IBIS/ISGRI count rates to X-ray luminosities (in the same energy range) have been derived from the analysis of IBIS/ISGRI spectra. We have extracted spectra from seven ScWs (or less for the two sources where seven detections were not reached) in which each source was within 12° from the centre and detected above 5σ in the IMA step. We verified that the spectra of these sources did not show strong evidence for variability and fitted the average spectra to obtain reliable conversion factors from source count rates to X-ray fluxes, in the same energy range. Different kinds of models have been adopted, in order to get a good deconvolution of the average spectra. We assumed the appropriate source distances to obtain the relative luminosities in each energy range. The final conversion factors for each band and the distances used are given in Table 5. We note that the main uncertainty in this process is relative to the source distances.

Table 5. Conversion factors from count rates (counts s^{-1}) to luminosities (erg s^{-1}). No value ('–') means that the source was never detected in the given energy band (namely 50–100 keV, see Table 2); 'n/a' means that the source was not extracted in the given band (only SFXTs have been extracted in 22–50 keV, see Section 6).

Name	Distance (kpc)	17–30 keV ($\times 10^{34}$)	30–50 keV ($\times 10^{34}$)	17–50 keV ($\times 10^{34}$)	22–50 keV ($\times 10^{34}$)	50–100 keV ($\times 10^{34}$)
Prototypical SFXTs						
XTE J1739−302	2.7	3.50	5.20	4.00	3.10	9.60
IGR J17544−2619	3.6	6.00	10.5	6.30	6.20	4.05
SAX J1818.6−1703	2	2.00	2.80	2.20	2.00	4.10
Intermediate SFXTs						
IGR J16418−4532	13	75.0	100.0	90.0	86.0	–
IGR J16479−4514	4.9	12.0	17.0	13.0	14.0	35.0
IGR J18483−0311	3	4.30	6.50	5.00	5.40	11.0
IGR J18450−0435	3.6	6.20	10.0	7.40	7.80	–
Less explored SFXTs						
IGR J16465−4507	9.5	41.0	54.0	49.0	46.0	–
IGR J08408−4503	2.7	3.57	4.98	3.94	4.14	–
IGR J18410−0535	3.2	4.95	7.43	5.66	5.94	–
The periodic SFXT						
IGR J11215−5952	6.2	18.6	26.8	21.0	22.6	–
HMXBs						
4U 1700−377	1.9	1.60	6.90	2.00	n/a	4.00
Vela X-1	1.8	1.40	2.90	1.90	n/a	4.30
4U 1907+09	4	7.60	15.0	8.70	n/a	–
Crab	2	2.00	3.00	2.20	n/a	5.30

5 CUMULATIVE LUMINOSITY DISTRIBUTIONS

Merging the results shown in the two previous sections, for each source we built the *complementary cumulative distribution function* (hereafter, only *cumulative distribution*) of the obtained X-ray luminosities. In each point of these functions, at a given luminosity L_X the sum of all events (detections) with a luminosity larger than L_X are plotted. The advantage of the cumulative distributions is that there is no need to arbitrarily bin the data, enabling a comparison between the different sources and avoiding loss of information.

Figs 1 to 4 show the resulting cumulative distributions for all the sources of our sample, in all the extracted bands. Each curve has been normalized to the total exposure time for which the source was within 12°. The source duty cycles, i.e. the percentage of time where the source is active with respect to the whole data base, can be seen in each plot as the highest value in the *y*-axis, and is given in Table 3 for the 17–50 and 17–30 keV bands. As can be seen, SFXTs have a few per cent duty cycle and are very soft, basically disappearing in the 50–100 keV band (Fig. 4).

In these plots, a perfectly constant source detected by an ideal detector would result in a vertical line. In our case, we see that the Crab source has a deviation from the straight line, towards lower luminosities. This is due to the combination of two effects: instrumental and intrinsic to the source. In a nine year operational period, IBIS/ISGRI response has changed, hence the resulting Crab light curve is not constant. The overall Crab count rate trend in 17–30 keV as obtained from the IMA analysis can be seen in Fig. 5, right-hand panel, in black. This effect, however, is clearly visible in the Crab because it is very bright, while it is washed away by the statistics in the other sources. Our overall observed variability (i.e. deviation from a vertical straight line in Figs 1 to 4) also includes the intrinsic ∼7 per cent flux decline that has been observed in the hard X-ray emission of the Crab, independently confirmed by several instruments, including IBIS in the 15–50 keV band (Wilson-Hodge et al. 2011). In the cumulative distributions no time information is retained, hence we cannot disentangle the two variabilities (instrumental versus intrinsic).

5.1 Comparing slow and fast variability

To have a better feeling of how the obtained distributions change according to the binning chosen (∼ ks versus 100 s in 17–30 keV), we show some examples where we plot in the same diagram the two different curves belonging to the same source. Figs 5–7, left-hand panels, show the Crab, IGR J16479−4514 and IGR J17544−2619, respectively. As it can be seen, in the case of the Crab the two curves (black for ScW IMA, and green for 100 s LCR) basically overlap. This is because the Crab is bright and stable, hence if we look at its light curve (Fig. 5, right-hand panel), we see that the distribution of the 100 s rates (green) is about symmetrically placed around the obtained, average, ScW value (black). Furthermore, the finer binning has a larger statistical scatter and this results in a broader coverage of the corresponding distribution, visible in the left-hand panel. We note that in the LCR-based distribution, unlike the IMA-based one, the Crab has a small high energy tail that deviates towards higher luminosities. This is due to six 100 s bins (out of a total of 68 246) that reach about 250 counts s^{-1}(Fig. 5, right-hand panel, in green). We expect the Crab to be the worst case scenario and even here the percentage of bins that deviate is negligible.

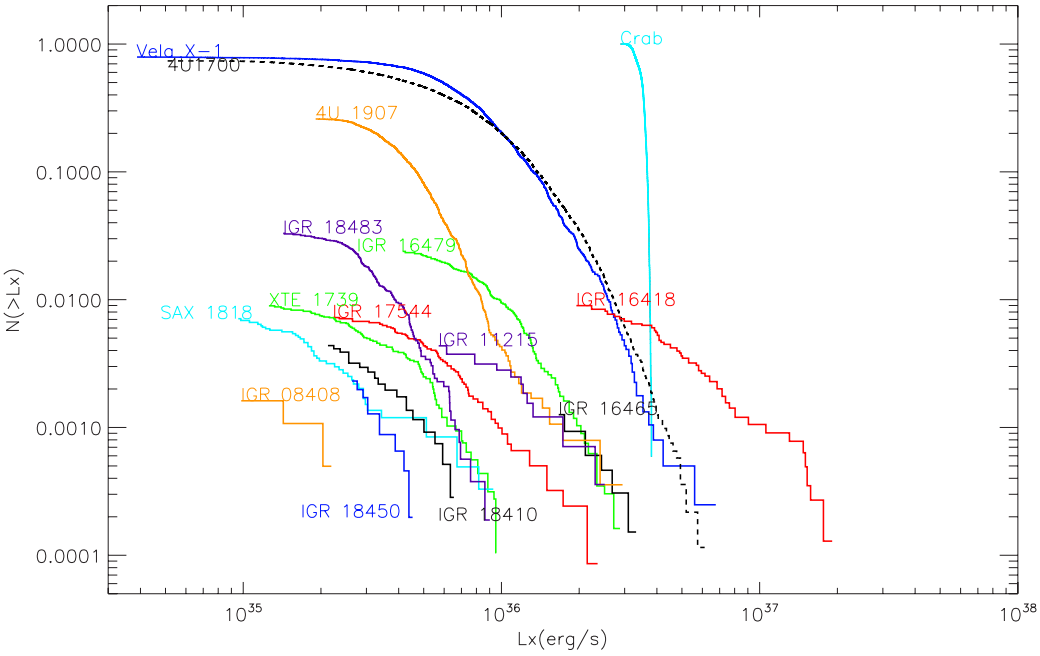

Figure 1. Cumulative luminosity distributions for all the sources of our sample in 17–30 keV, as obtained from the imaging analysis (∼ks bins). Each curve has been normalized to the total exposure time for which the source was within 12° (Table 2). The duty cycles, the highest values in the *y*-axis, are with respect to the whole archive and are given in Table 3 for the 17–30 keV band shown here and for the 17–50 keV band shown in Fig. 3.

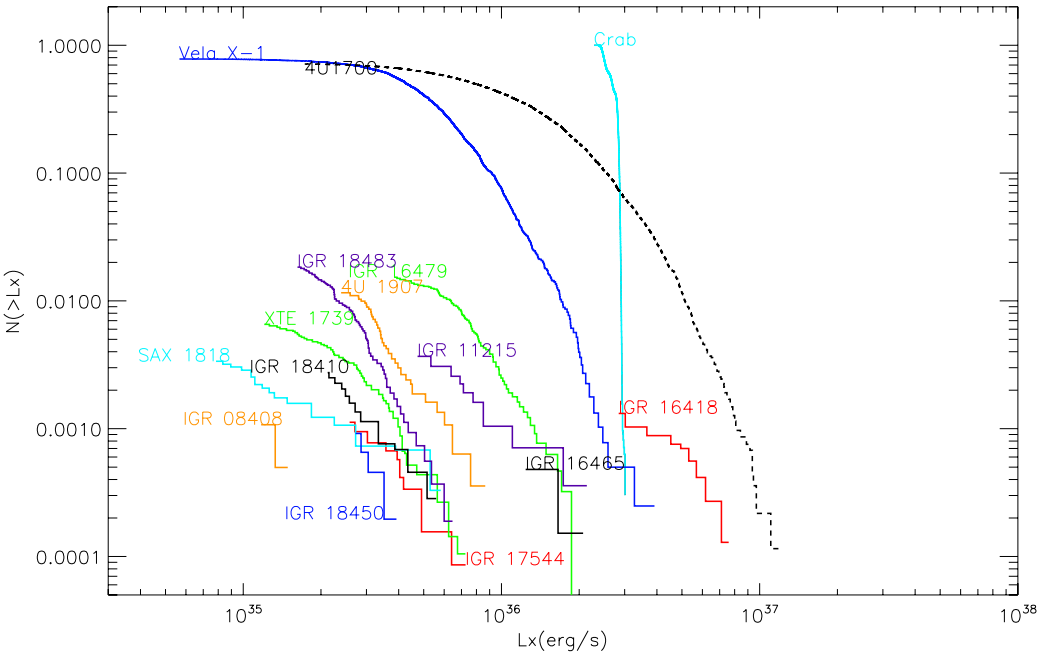

Figure 2. As in Fig. 1 but for 30–50 keV.

For IGR J16479−4514 and IGR J17544−2619, the two cumulative distributions do not overlap (Figs 6 and 7, left-hand panels). Indeed the 100 s cumulative curves (green in the left-hand panels) lie at higher luminosities than those obtained from the ScW average (black). This is because the sources are fainter and lie closer to the detection threshold, hence, the bins in which we consider a detection, $>3\sigma$, are the brightest in the corresponding light curves (green in the right-hand panels). On the contrary, the bins with detection lower than 3σ are rejected (shown in red) and are not included in the LCR curves of the left-hand panels, but they still contribute to build the average IMA value (black). While the shift of the cumulative distributions to higher luminosities (increasing *x*-axis) from IMA to LCR is due to the 3σ selection effect, the shift towards a higher percentage (increasing *y*-axis) is due to the fact that the LCR duty cycles are not with respect to the whole nine year archive, as IMA, but with respect to when the source was active in the IMA step (i.e. LCR duty cycles are higher than the IMA ones).

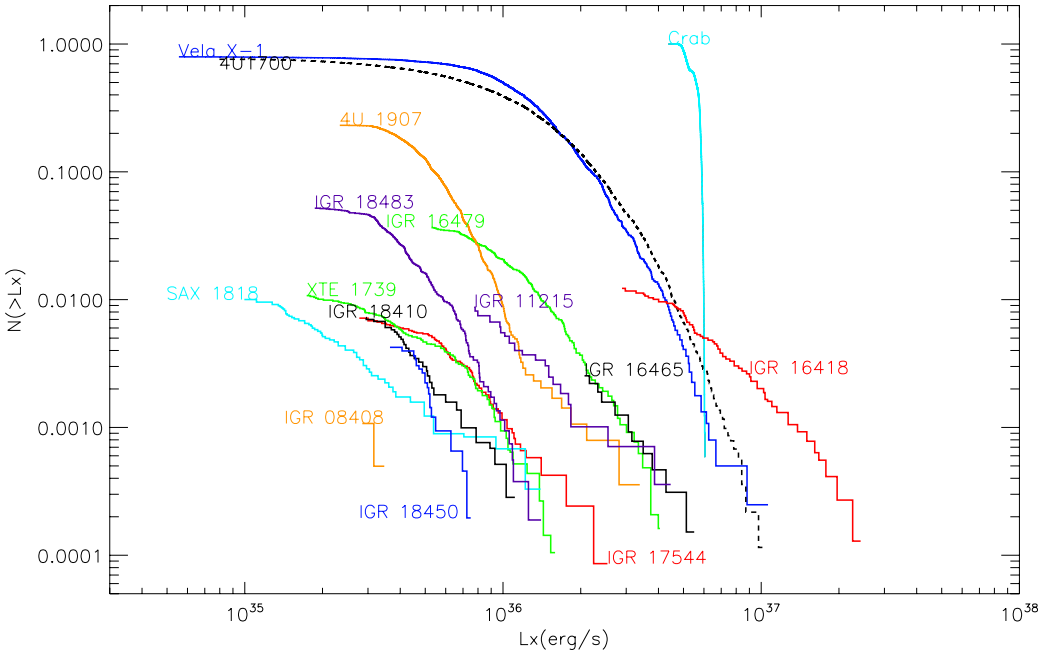

Figure 3. As in Fig. 1 but for 17–50 keV.

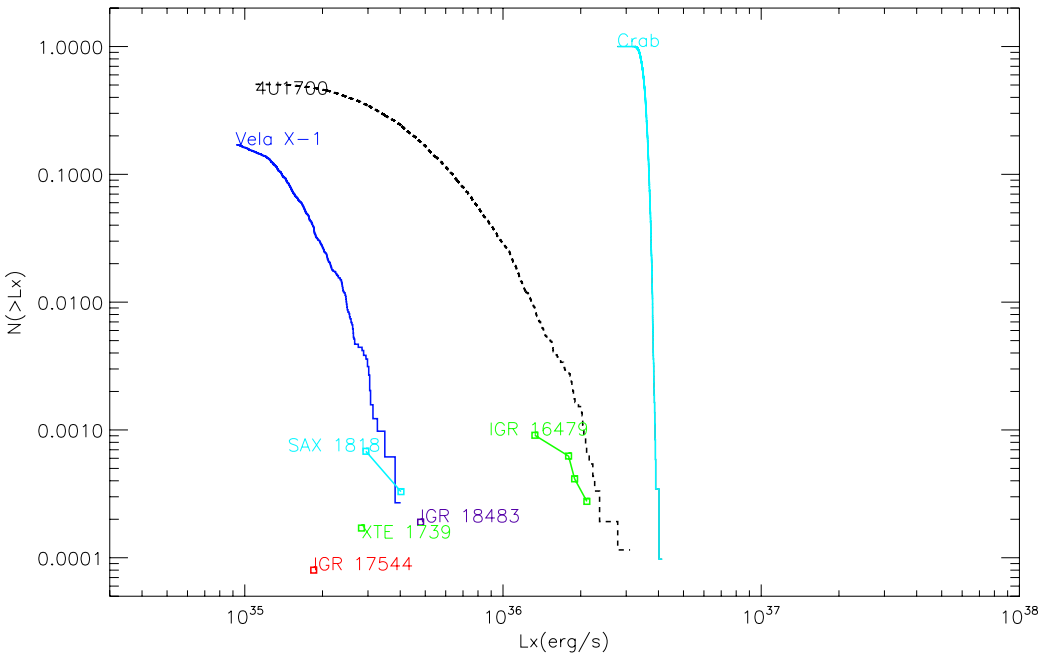

Figure 4. As in Fig. 1 but for 50–100 keV.

6 SFXTs, A NEW EXTRACTION IN 22–50 keV

We initially adopted a low energy boundary of 17 keV to maximize the detections with IBIS/ISGRI. However, the efficiency of IBIS/ISGRI fluctuates with the lower energy threshold, so that the detector response is not stable. In the case of the SFXTs of our sample, about 80 per cent of the detections occur before revolution 848, where the low energy threshold (LT) of IBIS/ISGRI fluctuates between about 16 and 19 keV (Caballero et al. 2012) hence for our purposes, the IBIS response can be considered basically stable. For the remaining 20 per cent of our detections, the efficiency of IBIS/ISGRI is not optimal in our chosen energy range and we may be underestimating the detected fluxes. We do not expect this to impact in an important way the results shown up to now: IMA and LCR results have been compared in the same band, the majority of our detections are before the increase of the LT, and we use the wide and most efficient 17–50 keV energy band to compute the duty cycles. In any case, the effect of the LT increase in IBIS/ISGRI is to eventually miss some detections in the 20 per cent portion of the data where the LT is between 20 and 22 keV.

We note, however, that since we intend to discuss the cumulative luminosity distributions, as a cross-check we have re-analysed all

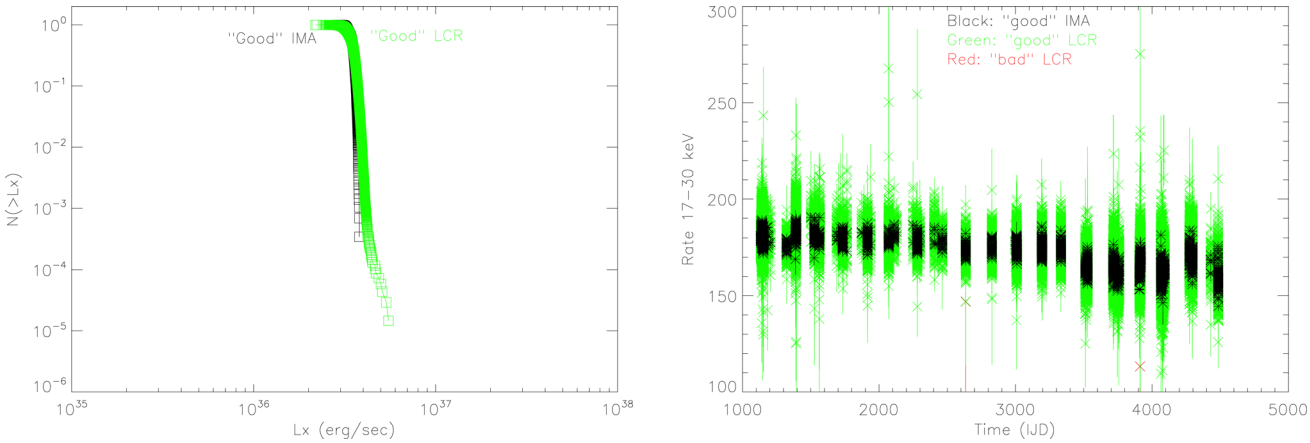

Figure 5. Left-hand panel: comparison of the Crab luminosity cumulative distributions, as obtained from IMA step (black) and LCR (green). A flatter slope indicates more variability. Right-hand panel: Crab light curve in the 17–30 keV band. Black: 'good' rate and error bars from IMA step (i.e. ∼ks bin detection above 5σ and off-axis angle $<12^{\circ}$). Green: 'good' rate and error bars from the LCR step (i.e. 100 s bin detection above 3σ within the 'good' IMA ScWs). Red: 'bad' rate and error bars from LCR step (i.e. detection below 3σ).

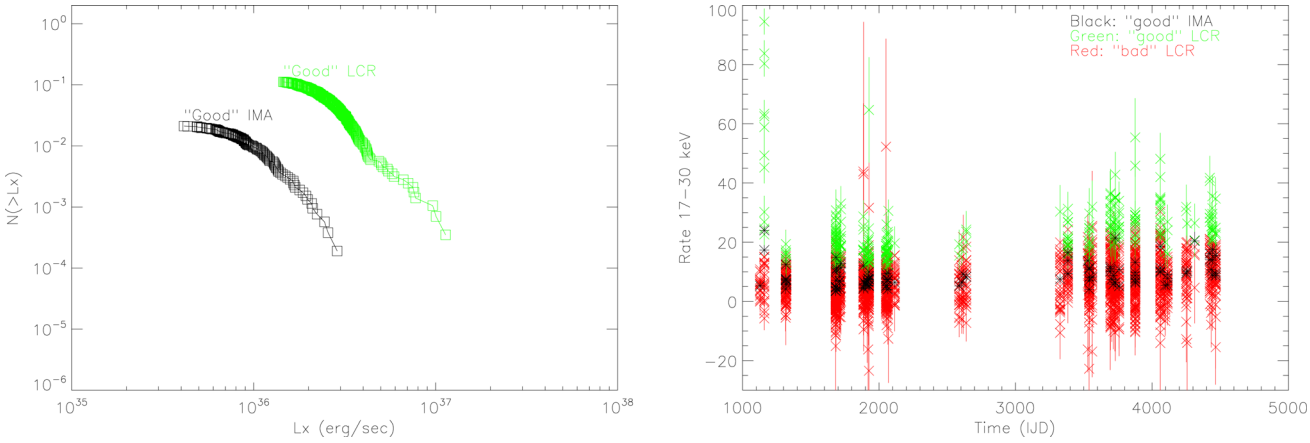

Figure 6. As in Fig. 5 but for IGR J16479−4514.

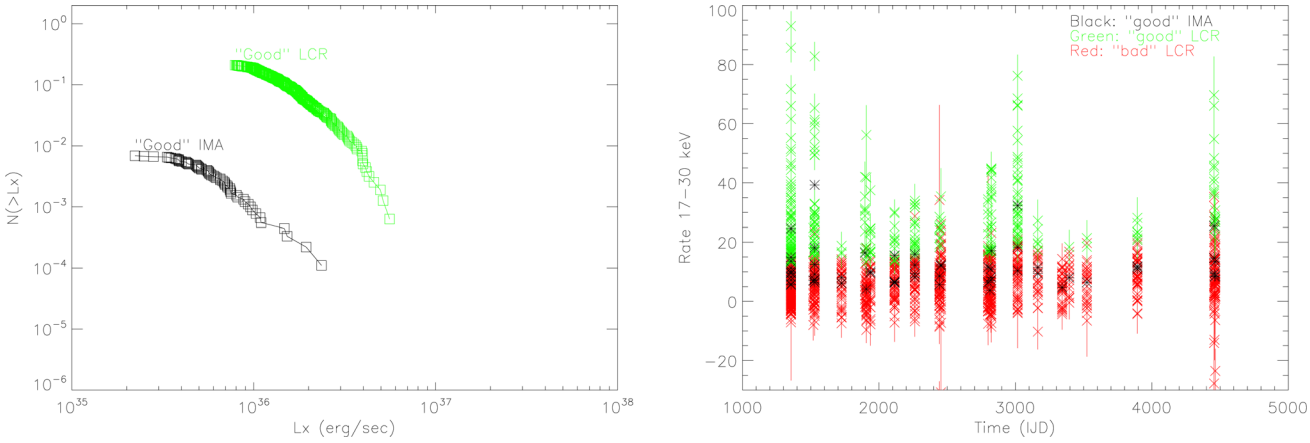

Figure 7. As in Fig. 5 but for IGR J17544−2619.

the ScWs for which the SFXTs have been detected in the 17–30 or 17–50 keV band, extracting images in the 22–50 keV band. Our results are hence free from LT fluctuations, but many detections are lost since we are not considering the 17–22 keV bit anymore (20 per cent of the detections less than the 17–50 keV range). Since this analysis considers a subsample of the whole archive (656 ScWs versus the complete archive, currently 90 491 ScWs), the duty cycles for this IMA step are arbitrary and will not be discussed any further.

A global view of our results is given in Table 6 while the newly extracted SFXT luminosity distributions are discussed in Section 7.

Table 6. Results from our 22–50 keV IMA analysis on SFXTs.

Name	Average rate[a] (counts s^{-1})	Detections[a] ks (#ScWs)	Minimum L_X ($\times 10^{35}$ erg s^{-1})	Maximum L_X ($\times 10^{35}$ erg s^{-1})	Mean L_X ($\times 10^{35}$ erg s^{-1})	Median L_X ($\times 10^{35}$ erg s^{-1})
Prototypical SFXTs						
XTE J1739−302	10.3 ± 0.1	135.3 (74)	1.1	8.6	3.2	2.8
IGR J17544−2619	7.9 ± 0.2	80.7 (48)	1.7	15.1	4.9	4.3
SAX J1818.6−1703	10.1 ± 0.2	55.4 (35)	0.8	8.6	2.0	1.5
Intermediate SFXTs						
IGR J16418−4532	7.2 ± 0.2	59.7 (38)	25.4	159.1	61.9	54.0
IGR J16479−4514	7.6 ± 0.1	240.4 (144)	4.0	31.2	10.6	9.5
IGR J18483−0311	7.2 ± 0.1	243.7 (156)	1.6	10.2	3.9	3.5
IGR J18450−0435	5.2 ± 0.2	19.8 (13)	2.8	6.2	4.1	3.7
Less explored SFXTs						
IGR J16465−4507	4.6 ± 0.3	12.4 (6)	14.32	35.2	21.2	22.8
IGR J08408−4503	5.5 ± 0.4	4.9 (2)	2.0	2.5	2.3	2.5
IGR J18410−0535	6.9 ± 0.2	32.2 (24)	2.3	8.2	4.1	3.6
The periodic SFXT						
IGR J11215−5952	5.5 ± 0.2	27.4 (15)	5.9	34.6	12.4	10.9

[a]We provide the exposure time, as well as the number of ScWs (#scws), in which an IMA significance >5 is obtained.

We anticipate here that, besides the percentage of detections, there is no qualitative difference between the 17–50 keV and 22–50 keV results, as far as our discussion is concerned.

7 CHARACTERIZING THE CUMULATIVE DISTRIBUTIONS

After building the cumulative distributions, we tried to characterize them in a more quantitative way, modelling them with a power law. Note that a striking feature is present in the cumulative distributions, i.e. a low luminosity turnover. In the case of SFXTs, this is due to the missing detections of faint flares near the sensitivity threshold of the detector, and is often observed in cumulative distributions in many different contexts (Clauset, Rohilla Shalizi & Newman 2009). This implies that the sampling is not complete *near* this low luminosity cutoff, and that only data points lying above a so-called *truncation point* can be considered in the estimation of the best power-law slope.

Sometimes, at the high end of the luminosity distribution, a turnover is observed as well. This can be due to a 'finite' size scaling caused by the fact that the system has a finite length-scale (a maximum luminosity in this case). Alternatively, it can be due to the fact that nine years of observations are not enough to catch the most extreme flares and cover all the statistics of the flaring activity from a given SFXT. This implies that the upper end of the SFXTs luminosity distributions is affected by larger uncertainties, because a few extreme events can significantly change the high luminosity tail.

To evaluate the power-law slope of the SFXTs cumulative distributions, we restricted our analysis to the energy band 17–50 keV (IMA results), to take advantage from the wider energy coverage and statistics (and to 22–50 keV for comparison). We adopted a maximum-likelihood estimation (MLE) of the power-law slope from a subsample of data points above a truncation point, different for each source (Crawford, Jauncey & Murdoch 1970). Since the resulting power-law slope is strongly dependent on the assumed lower bound, we obtained the best truncation point empirically, by optimizing the Kolmogorov–Smirnov (KS) goodness-of-fit statistics (Clauset et al. 2009): for each source, at first a truncation point for the lowest luminosity value in the cumulative distribution is assumed; then an MLE method has been applied to obtain the power-law slope and a KS test is performed. This loop is repeated increasing the value of the truncation point. Finally, we chose as the correct value for the truncation point the one which makes the probability distributions of the measured data and the best-fitting power-law model as similar as possible above that particular truncation point.

The results obtained with this method are reported in Table 7 for all the sources except the two that have too few detection (the less explored SFXTs, IGR J16465−4507 and IGR J08408−4503). We list the final truncation point adopted for each cumulative distribution, the number of data points used (together with the initial total number of data points) and the best power-law slope obtained. The corresponding KS probability is also listed.

Fig. 8 shows some examples of power-law fits to the cumulative distributions for the three typical cases: single power-law fit for most of the data (after the truncation point, upper panels), two power-law fit for most of the data (after the truncation point, lower-left panel) and single power-law fit for a very limited fraction of the data (the high energy tail, lower-right panel).

In Fig. 9 we show the power-law slopes that better model the cumulative luminosity distribution functions in the energy range 17–50 keV (black crosses) and in the energy band 22–50 keV (red squares). For classical HMXBs we have only the results in the 17–50 keV range. A very good agreement is found between the power-law slopes estimated in the two IBIS/ISGRI energy bands. Hence the effect of the instrumental LT fluctuations up to 22 keV plays a role in the percentage of detections alone, with no further bias involved.

We note also that in case of SFXTs, a good fit with a power law is obtained considering a large subsample (>80 per cent) of the original data points (SAX J1818.6−1703, IGR J18410−0535 and IGR J11215−5952; in this latter source 100 per cent of the data points follow a power-law model). The classical HMXBs however, behave very differently: a power-law model is a good fit only for the high luminosity tail of the distribution (involving less than 0.5, 1.6 and 20 per cent of the total data points for Vela X-1, 4U 1700−377 and

Table 7. MLE of the power-law parameters of the cumulative luminosity distributions (17–50 keV).

Name	Truncation point L_X (10^{35} erg s^{-1})	#ScWs (tot #ScWs)	Power-law slope	KS probability
Prototypical SFXTs				
XTE J1739−302	6.3	32 (87)	2.16 ± 0.56	0.984
IGR J17544−2619	6.5	31 (64)	2.73 ± 0.61	0.953
SAX J1818.6−1703	1.4	41 (46)	1.39 ± 0.28	0.993
Intermediate SFXTs				
IGR J16418−4532	52.0	36 (57)	1.31 ± 0.31	0.997
IGR J16479−4514	14.6	52 (172)	2.36 ± 0.47	0.996
IGR J18483−0311	3.6	139 (200)	2.28 ± 0.26	0.962
	6.7	30 (200)	4.06 ± 0.97	0.979
IGR J18450−0435	4.48	15 (16)	4.1 ± 1.6	0.861
Less explored SFXTs				
IGR J18410−0535	3.8	24 (29)	2.20 ± 0.65	0.899
The periodic SFXT				
IGR J11215−5952	–	19 (19)	1.35 ± 0.45	0.885
HMXBs				
4U 1700−377	45.0	83 (5285)	4.10 ± 0.57	0.891
Vela X-1	45.0	10 (1970)	4.1 ± 1.2	0.958
4U 1907+09	6.56	210 (815)	4.10 ± 0.29	0.721

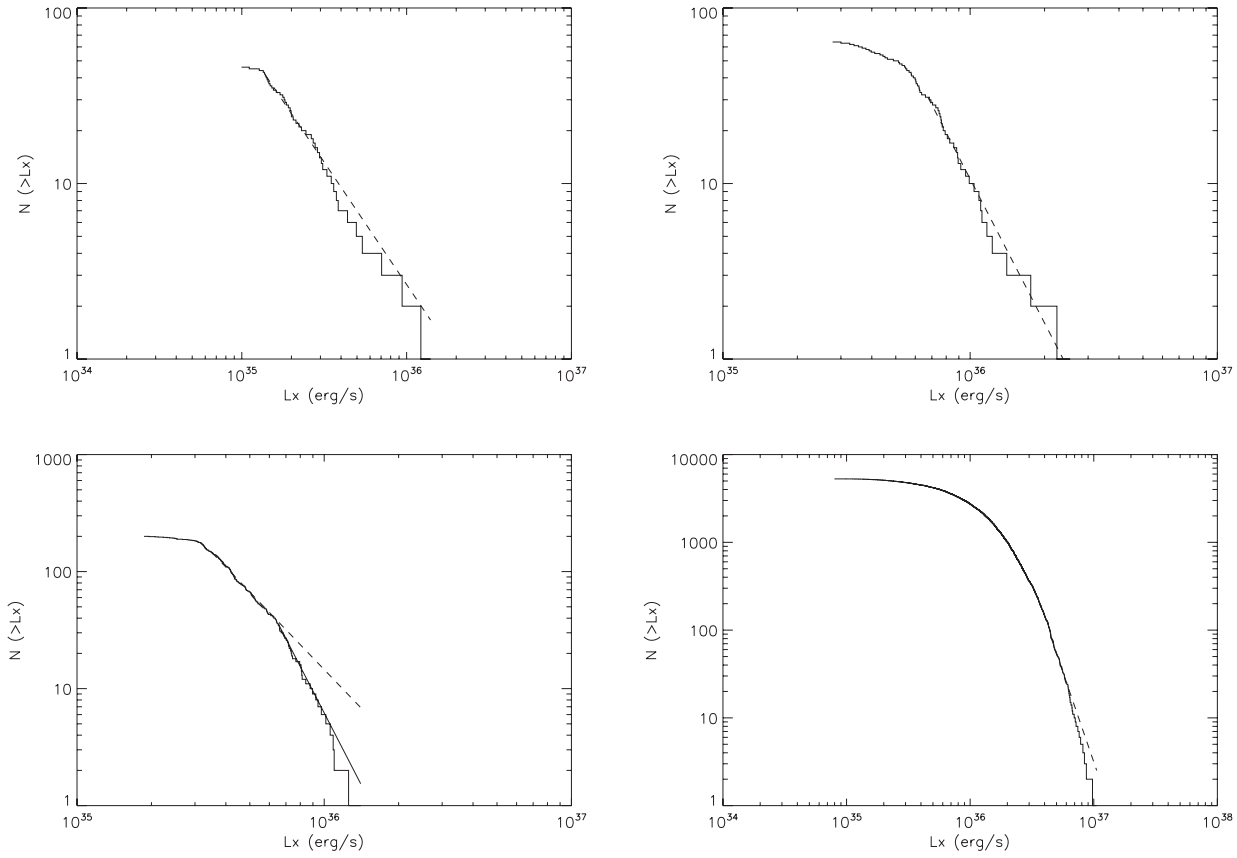

Figure 8. Examples of power-law fits (dashed lines) to the non-normalized cumulative luminosity distributions (17–50 keV; solid lines) of four sources: two prototypical SFXTs (SAX J1818.6−1703, upper left; IGR J17544−2619, upper right), the intermediate SFXT IGR J18483−0311 (lower left, with two power laws, before and after a break) and the classical HMXB 4U 1700−377 (lower-right panel), where only the tail is power-law like.

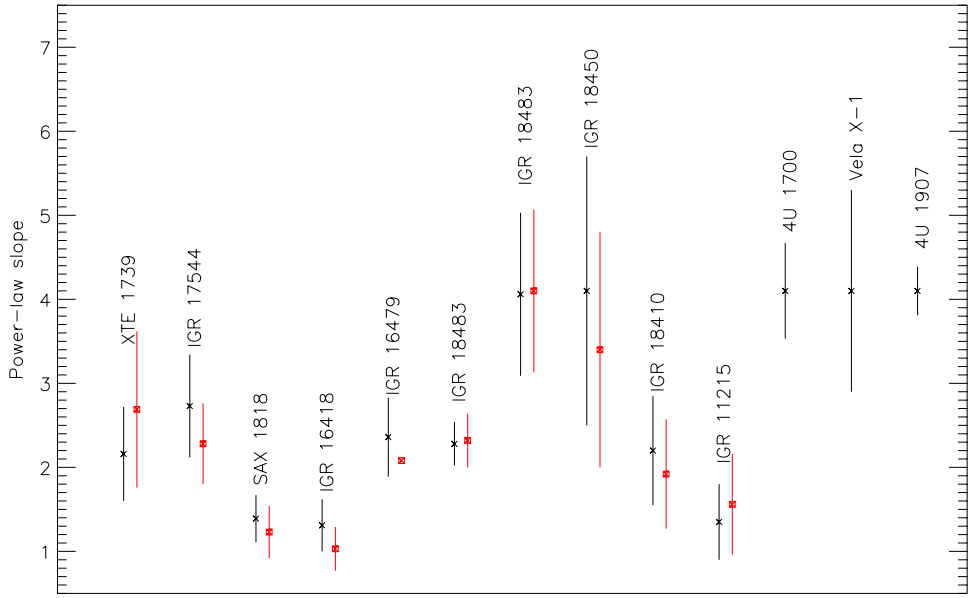

Figure 9. Results of the MLE of the power-law parameters of the cumulative luminosity distributions in the energy band 17–50 keV (crosses) and in the 22–50 keV (squares), for comparison.

4U 1907+09, respectively). We note that their power-law slope is always around 4. Apart from IGR J18450−0435, for which the sample is small and the uncertainty on the power-law slope is large, the source IGR J18483−0311 also displays a behaviour which shares some similarity with the classical HMXBs: its cumulative distribution appears to show a break at about 6.7×10^{35} erg s^{-1}, with a slope of 2.28 ± 0.26 before it (more in line with the flatter power laws shown by other SFXTs) and a slope of 4.06 ± 0.97 above it (compatible with the tail in the classical HMXBs). This quantitatively confirms the intermediate character of this SFXT (Rahoui & Chaty 2008).

We are aware that for some sources the sample used for MLE of the power-law exponent is small, and that a high KS probability does not imply that the data are truly drawn from a power-law distribution. However, these quantitative estimations confirm and better quantify what was already evident from the visual inspection of the cumulative distributions: SFXTs are more power-law like (and with a flatter slope) in their cumulative luminosity distributions with respect to the classical HMXBs, with SAX J1818.6−1703 and IGR J12215−5952 being the best cases of power-law like distribution.

Since the luminosity distributions of 4U 1700−377 and Vela X-1 are completely different from those shown by other sources, and since the power-law fit in their case can account for only the high luminosity tail, we tried to fit their 17–50 keV curved shape with the cumulative distribution expected from a log-normal function. Indeed, a log-normal function was found to fit well the X-ray brightness distribution of Vela X-1 by Fürst et al. (2010), using *INTEGRAL* data (20–60 keV). In our case, MLE of the parameters of the cumulative distribution for a log-normal function resulted in a median luminosity of 1.2×10^{36} and 1.1×10^{36} erg s^{-1} (with a multiplicative standard deviation, σ, of 0.542 and 0.688) for Vela X-1 and 4U 1700−377, respectively (Fig. 10). The best truncation points for the two cases were 2.75×10^{35} erg s^{-1} (Vela X-1, implying 1909 out of 1970 data points) and 2.67×10^{35} erg s^{-1} (4U 1700−377, implying 4903 out of 5285 data points). Note however that in our case a log-normal can be rejected (KS probability of 0.408 and 0.0225 for Vela X-1 and 4U 1700−377, respectively).

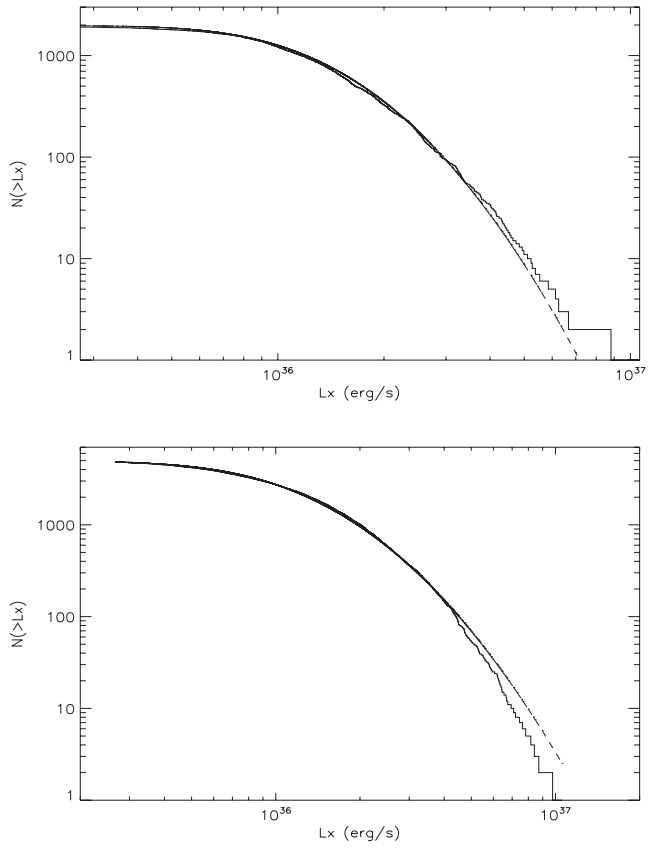

Figure 10. Examples of the best log-normal functions (dashed lines) fitted to the Vela X-1 (upper panel) and 4U 1700−377 (lower panel) non-normalized cumulative luminosity distributions (solid lines; 17–50 keV). See the text for the details and the resulting parameters.

Indeed, although a log-normal may be a plausible representation of data spanning a short period of time (as in Fürst et al. 2010, *INTEGRAL* revolutions 0433–0440), this is not the case when a wider data base is considered (as in this work, where Vela X-1

detections spanning revolutions 0028–1138 are considered). This can be explained by the presence of long-term trends in nine years of *INTEGRAL* data, trends that are clearly visible in the case of persistent and bright sources (such as Vela X-1 or the already discussed Crab), but buried within the highly variable emission and more sporadic detections of SFXTs.

We will not discuss this further, since the detailed investigation of the exact shape of the cumulative distributions in these two persistent sources is beyond the scope of our paper.

8 DISCUSSION

IBIS/ISGRI is able to catch bright SFXT flares that represent the most extreme events in HMXBs hosting NS. The temporal profiles of SFXT flares are usually very complex (e.g. Sidoli 2010) so it is problematic to define an *X-ray flare* given also the ambiguity in clearly separating overlapping single flares. Since time-scales of flare durations are roughly consistent with a ScW duration, we decided to consider the single IBIS/ISGRI detections on ScW level (IMA results; $\sim$ ks sampling) as a good representation of SFXT flares. SFXT flares are intermittent with a duration much shorter than the time interval between two adjacent major outbursts (typically a few months). An outburst is composed of several flares with different peak luminosity, duration and temporal profile. Their occurrence cannot be a priori predicted, except for the periodic SFXT IGR J11215−5952 (Sidoli et al. 2006), where the periodically recurrent outbursts are believed to trace the orbital period of the system.

Using the whole *INTEGRAL* archive available to date (spanning about nine years), we have built the cumulative distributions of the luminosity of all known SFXTs, and compared them with classical HMXBs. For the first time, we have quantitatively characterized such distributions for the SFXTs, deriving their duty cycles, dynamic range and typical luminosity in bright flaring activity. Indeed, the cumulative distributions show many aspects of the behaviour of sources at hard X-rays, when comparing SFXTs to the other three HMXBs. In Fig. 3 we have shown the cumulative luminosity distributions at IMA level in the energy range 17–50 keV, which is the most comprehensive (and with the best statistics) at IMA level. On the *x*-axis the range of variability (the dynamic range as observed by IBIS/ISGRI) covered by each source is evident, together with the threshold in X-ray luminosity above which *INTEGRAL* can observe each source, assuming that the distances are correct. On the *y*-axis, the percentage of time spent above the threshold of detectability by the different sources can be derived. Clearly different behaviours can be seen from these cumulative distributions. Vela X-1 and 4U 1700−377 are always detected except during X-ray eclipses or the so-called off-states (Kreykenbohm et al. 2008). Their most frequent state is at high luminosity, around 1–2 $\times$ 10^{36} erg s^{-1}. The transient HMXB 4U 1907+09 distribution is located below them, implying a duty cycle of $\sim$20 per cent, intermediate between the persistent HMXBs (Vela X-1 and 4U 1700−377) and the *intermediate* SFXTs IGR J18483−0311 and IGR J16479−4514 (with a duty cycle of $\sim$4–5 per cent). This confirms the (not so) transient behaviour previously reported for this source (Doroshenko et al. 2012).

Orbital and superorbital modulations of the source X-ray light curves could, in principle (as any other periodic or aperiodic trend), affect the shape of the cumulative luminosity distributions. However, considering both the nature of the sources in our study and the *INTEGRAL* sensitivity (able to catch only the bright flares), the effect of the amplitude of the orbital and superorbital modulations is negligible when compared to the X-ray luminosity variability produced by the SFXTs X-ray flares. A similar conclusion holds also for the cumulative luminosity distributions of persistent HMXBs, but for a different reason: here the orbital modulations are due to the presence of X-ray eclipses, during which the sources are not detected with *INTEGRAL*, so that the eclipses do not produce any effect in the cumulative distributions.

The sources with the lowest IMA-based duty cycle are confirmed to be the *prototypical SFXTs* together with some less explored SFXTs and the periodic SFXT IGR J11215−5952.[5] However, when we consider the short-term variability (100 s, Table 4) we note that the prototypical SFXTs are detected more than 20 per cent of the times, while the intermediate ones reach about 14 per cent at most (17 per cent at most for the less explored SFXTs). This result holds also if we increase the LCR detection threshold to the more conservative 5σ level, with the prototypical SFXTs being around 8 per cent and the remaining (intermediate and less explored) SFXTs being below 1 per cent (the only exception being IGR J08408−4503 that reaches 6 per cent). This result does not depend on the number of detections in the IMA step (i.e. more detections in IMA resulting in more detections in LCR), since, for example, IGRJ 16479−4514 has 111 detections at a ScW level (Table 2) and 11 per cent of detections in LCR (Table 4), while XTE J1739−302 has only 70 detections at a ScW level and about 27 per cent of detections in LCR. Furthermore, this difference is unlikely due to statistics alone (i.e. the brightest sources having the highest detection percentage in 100 s) since, as can be seen from Table 2, there is not a clear and linear behaviour in the sources, e.g. IGR J18410−0535 has an IMA average count rate of 8 $\pm$ 0.3 counts s^{-1}and an LCR detection of 17 per cent, while IGR J16418−4532 has an IMA average rate of 9 $\pm$ 0.3 counts s^{-1}and an LCR detection of 7 per cent. Hence it is likely that we are seeing a real difference within the subgroups of SFXTs: when investigating how the 100 s bins are distributed within the 'good ' ScWs, we find that the intermediate SFXTs seem to be more constant, with most weak bins giving the detection in a ScW, while the prototypical ones are more variable, with more flaring bins that lead to the detection at a ScW level.

The cumulative distributions of most of the SFXTs analysed here can plausibly be considered to follow a power-law function. The power-law slope of the cumulative distributions for the three prototypical SFXTs also agrees with the one previously found with PCA/*RXTE* data (Smith et al. 2012). Although Smith and collaborators perform only a rough estimate of the power law (slope of 1.5, with no uncertainty), the slopes we found for the three prototypical SFXTs at hard X-rays with *INTEGRAL* seem to be consistent with the power-law like luminosity distribution derived at soft X-rays (2–10 keV). Although the X-ray luminosity range covered by SFXTs in our study is about two orders of magnitude, being the luminous outbursts covered, a plausible fit with a power law of their cumulative luminosity distributions is reminiscent of Self-Organized Criticality (SOC) Systems (e.g. Aschwanden 2013, and references therein). An SOC (Bak, Tang & Wiesenfeld 1987) is a system which naturally and perpetually evolves into a critical state where a minor event can start a chain reaction leading to a catastrophe, like in a sandpile, where even though sand is uniformly added to the pile, the amount of sand falling from the pile can greatly vary with time, giving rise to unpredictable 'avalanches' when a certain instability threshold is reached. Several phenomena, not only in nature but also in human

[5] We note that the distance to IGR J16418−4532 is not very constrained ($\sim$13 kpc), so its position along the *x*-axis is not well known, and could be shifted to lower luminosities.

systems, are believed to behave like SOC systems: earthquakes, landslides, solar flares, forest fires and lunar craters (e.g. Newman 2005).

The power-law scaling of SFXTs cumulative luminosity distributions, a necessary but not sufficient condition for an SOC system, is remarkable. We suggest that SFXTs flares can be possibly considered as 'avalanches' in SOC systems, which are triggered when a critical state is reached. In our case, accretion can be interpreted as the slow and steady driver towards the critical state required to the SOC system to produce the avalanche.

Recently, Shakura et al. (2012) proposed a new model to explain quasi-spherical accretion of matter in HMXBs with NS and supergiant companions, and it has been successfully applied to SFXTs by Drave et al. (2014). In this model, if the source is in a low luminosity state (<3–5×10^{35}erg s^{-1}), the wind matter captured by the NS within the Bondi radius cannot efficiently cool down by Compton processes; a hot shell forms between the Bondi radius and the magnetospheric radius, accumulating above the NS magnetosphere. This matter penetrates the magnetosphere *only* if it is able to cool down to a critical temperature, so that Rayleigh–Taylor instability can allow high accretion rates on to the NS. When this critical temperature is reached, if a considerable amount of matter has already accumulated in the hot shell, it can suddenly accrete on to the NS producing SFXTs outbursts. In this respect, we suggest that this critical temperature can act as the threshold needed to start the intermittent 'avalanche' in an SOC system. This is very different from the persistent and bright HMXBs case, where a high photon flux allows the matter to efficiently cool down thanks to Compton cooling, maintaining high accretion rates.

9 CONCLUSION

We used about nine years of publicly available *INTEGRAL* observations to study in a systematic way all known SFXTs and three classical HMXBs. We have built the cumulative luminosity distributions and, for the first time for SFXTs, we have quantitatively characterized them. We derived duty cycles, dynamic ranges, slow versus fast variability properties and typical luminosities during bright flaring activity.

We characterized the cumulative luminosity distributions with a power-law model. We found that the X-ray luminosity range where the model is a plausible representation of the data is larger for SFXTs than for persistent HMXBs (where a power law is able to reproduce only the very high luminosity tail). Furthermore, SFXTs show a significantly flatter power-law slope than HMXBs.

We suggest that this power-law like behaviour is a possible indication of SOC and that SFXTs flares could be associated with avalanching resulting in an SOC system when an instability threshold is reached.

Among the several different explanations suggested for SFXTs, the Shakura et al. (2012) model for quasi-spherical accretion seems, to date, to better explain SFXTs and their link with persistent systems (see Drave et al. 2014 for the application to SFXTs). It predicts the complete collapse of a hot shell of gravitationally captured wind material accumulated above the NS magnetosphere, when it cools below the critical temperature, allowing the onset of Rayleigh–Taylor instability.

While persistent accreting pulsars spend most of their life in an efficient Compton cooling regime which allows (and is permitted by) high X-ray luminosities (10^{36}erg s^{-1}), SFXTs spend most of the time at much lower luminosities (10^{33}–10^{34} erg s^{-1}; Sidoli et al. 2008) where gravitationally captured matter accumulates above the NS magnetosphere and remains too hot to accrete at high rates. At these low X-ray luminosities, the matter is subject only to inefficient radiative cooling which allows a low accretion rate through the NS magnetosphere. At some point, the X-ray luminosity produced by this inefficient accretion can reach the critical X-ray luminosity which is able to trigger efficient Compton cooling of the matter below the critical temperature. This produces the onset of Rayleigh–Taylor instabilities and the complete collapse of the accumulated hot shell, giving rise to a SFXT outburst.

To conclude, we suggest that SFXTs power-law like cumulative luminosity distributions are possibly the consequence of a threshold-nature instability, supporting the Shakura et al. (2012) model for quasi-spherical settling accretion regime.

ACKNOWLEDGEMENTS

Based on observations with *INTEGRAL*, an ESA project with instruments and science data centre funded by ESA member states (especially the PI countries: Denmark, France, Germany, Italy, Spain, and Switzerland), Czech Republic and Poland, and with the participation of Russia and the USA. This work has made use of the *INTEGRAL* archive developed at INAF-IASF Milano, http://www.iasf-milano.inaf.it/~ada/GOLIA.html. We acknowledge the Italian Space Agency financial support *INTEGRAL* ASI/INAF agreement n. 2013-025.R.0. AP and LS thank Tony Bird, Massimo Cocchi, Mariateresa Fiocchi, Aleksandra Gros, Sandro Mereghetti, Lorenzo Natalucci and Jerome Rodriguez for useful discussions.

REFERENCES

Ankay A., Kaper L., de Bruijne J. H. J., Dewi J., Hoogerwerf R., Savonije G. J., 2001, A&A, 370, 170
Aschwanden M. J., 2013, preprint (arXiv:1310.4191)
Bak P., Tang C., Wiesenfeld K., 1987, Phys. Rev. Lett., 59, 381
Bird A. J., Bazzano A., Hill A. B., McBride V. A., Sguera V., Shaw S. E., Watkins H. J., 2009, MNRAS, 393, L11
Blay P. et al., 2008, A&A, 489, 669
Caballero I. et al., 2012, Proc Sci., INTEGRAL IBIS/ISGRI energy calibration in OSA 10. SISSA, Trieste, PoS(INTEGRAL 2012)142
Chaty S., Rahoui F., Foellmi C., Tomsick J. A., Rodriguez J., Walter R., 2008, A&A, 484, 783
Clark D. J., Hill A. B., Bird A. J., McBride V. A., Scaringi S., Dean A. J., 2009, MNRAS, 399, L113
Clark D. J. et al., 2010, MNRAS, 406, L75
Clauset A., Rohilla Shalizi C., Newman M. E. J., 2009, SIAM Rev., 51, 661
Coe M. J., Fabregat J., Negueruela I., Roche P., Steele I. A., 1996, MNRAS, 281, 333
Corbet R. H. D., Krimm H. A., 2013, ApJ, 778, 45
Corbet R. et al., 2006, The Astron. Telegram, 779
Cox N. L. J., Kaper L., Mokiem M. R., 2005, A&A, 436, 661
Crawford D. F., Jauncey D. L., Murdoch H. S., 1970, ApJ, 162, 405
Doroshenko V., Santangelo A., Ducci L., Klochkov D., 2012, A&A, 548, A19
Drave S. P., Clark D. J., Bird A. J., McBride V. A., Hill A. B., Sguera V., Scaringi S., Bazzano A., 2010, MNRAS, 409, 1220
Drave S. P., Bird A. J., Townsend L. J., Hill A. B., McBride V. A., Sguera V., Bazzano A., Clark D. J., 2012, A&A, 539, A21
Drave S. P., Bird A. J., Goossens M. E., Sidoli L., Sguera V., Fiocchi M., Bazzano A., 2013, The Astron. Telegram, 5131
Drave S. P., Bird A. J., Sidoli L., Sguera V., Bazzano A., Hill A. B., Goossens M. E., 2014, MNRAS, preprint (arXiv:1401.3570)
Fürst F. et al., 2010, A&A, 519, A37
Goldwurm A. et al., 2001, in Battrick B., ed., ESA SP-459, Exploring the Gamma-Ray Universe. ESA, Noordwijk, p. 497

Goldwurm A. et al., 2003, A&A, 411, L223
Goossens M. E., Bird A. J., Drave S. P., Bazzano A., Hill A. B., McBride V. A., Sguera V., Sidoli L., 2013, MNRAS, 434, 2182
Hong J., Hailey C. J., 2004, ApJ, 600, 743
Jain C., Paul B., Dutta A., 2009, MNRAS, 397, L11
Kreykenbohm I. et al., 2008, A&A, 492, 511
La Parola V., Cusumano G., Romano P., Segreto A., Vercellone S., Chincarini G., 2010, MNRAS, 405, L66
Labanti C. et al., 2003, A&A, 411, L149
Lebrun F. et al., 2003, A&A, 411, L141
Levine A. M., Corbet R., 2006, The Astron. Telegram, 940
Leyder J.-C., Walter R., Lazos M., Masetti N., Produit N., 2007, A&A, 465, L35
Lorenzo J., Negueruela I., Norton A. J., 2010, in Martí J., Luque-Escamilla P. L., Combi J. A., eds, ASP Conf. Ser. Vol. 422, High Energy Phenomena in Massive Stars. Astron. Soc. Pac., San Francisco, p. 259
Lund N. et al., 2003, A&A, 411, L231
McClintock J. E. et al., 1976, ApJ, 206, L99
Makishima K., Kawai N., Koyama K., Shibazaki N., Nagase F., Nakagawa M., 1984, PASJ, 36, 679
Marshall N., Ricketts M. J., 1980, MNRAS, 193, 7P
Mas-Hesse J. M. et al., 2003, A&A, 411, L261
Masetti N. et al., 2006, A&A, 449, 1139
Megier A., Strobel A., Galazutdinov G. A., Krełowski J., 2009, A&A, 507, 833
Negueruela I., Smith D. M., 2006, Astron. Telegram, 831
Negueruela I., Smith D. M., Chaty S., 2005, Astron. Telegram, 470, 1
Negueruela I., Smith D. M., Reig P., Chaty S., Torrejón J. M., 2006a, in Wilson A., ed., ESA SP-604, El Escorial – Madrid, Spain, Proceedings of The X-ray Universe 2005. ESA, Noordwijk, p. 165
Negueruela I., Smith D. M., Harrison T. E., Torrejón J. M., 2006b, ApJ, 638, 982
Negueruela I., Torrejón J. M., Reig P., 2008, Proc Sci., Optical and Infrared characterisation of High Mass X-ray Binaries discovered by INTEGRAL. SISSA, Trieste, PoS(Integral08)072
Nespoli E., Fabregat J., Mennickent R. E., 2008, A&A, 486, 911
Newman M., 2005, Contemp. Phys., 46, 323
Paizis A., Mereghetti S., Götz D., Fiorini M., Gaber M., Regni Ponzeveroni R., Sidoli L., Vercellone S., 2013, Astro. Comput., 1, 33
Pellizza L. J., Chaty S., Negueruela I., 2006, A&A, 455, 653
Rahoui F., Chaty S., 2008, A&A, 492, 163
Rahoui F., Chaty S., Lagage P.-O., Pantin E., 2008, A&A, 484, 801
Romano P., Sidoli L., Mangano V., Mereghetti S., Cusumano G., 2007, A&A, 469, L5
Romano P. et al., 2009, MNRAS, 399, 2021
Sguera V. et al., 2005, A&A, 444, 221
Sguera V. et al., 2007, A&A, 467, 249
Sguera V. et al., 2008, A&A, 487, 619
Shakura N., Postnov K., Kochetkova A., Hjalmarsdotter L., 2012, MNRAS, 420, 216
Sidoli L., 2010, Proc Sci., Supergiant Fast X-ray Transients (invited talk). SISSA, Trieste, PoS(Texas2010)082
Sidoli L., 2013, Proc Sci., Supergiant Fast X-ray Transients: a review. SISSA, Trieste, PoS(INTEGRAL2012)011
Sidoli L., Paizis A., Mereghetti S., 2006, A&A, 450, L9
Sidoli L., Romano P., Mereghetti S., Paizis A., Vercellone S., Mangano V., Götz D., 2007, A&A, 476, 1307
Sidoli L. et al., 2008, ApJ, 687, 1230
Sidoli L., Mereghetti S., Sguera V., Pizzolato F., 2012, MNRAS, 420, 554
Smith D. M., Markwardt C. B., Swank J. H., Negueruela I., 2012, MNRAS, 422, 2661
Swank J. H., Smith D. M., Markwardt C. B., 2007, The Astron. Telegram, 999
Torrejón J. M., Negueruela I., Smith D. M., Harrison T. E., 2010, A&A, 510, A61
Ubertini P. et al., 2003, A&A, 411, L131
Vedrenne G. et al., 2003, A&A, 411, L63
Wilson-Hodge C. A. et al., 2011, ApJ, 727, L40
Winkler C. et al., 2003, A&A, 411, L1
Winkler C., Diehl R., Ubertini P., Wilms J., 2011, Space Sci. Rev., 161, 149
Zurita Heras J. A., Chaty S., 2009, A&A, 493, L1

This paper has been typeset from a TEX/LATEX file prepared by the author.